

Article

Numerical Simulation and Experimental Verification of the Quenching Process for Ti Microalloying H13 Steel Used to Shield Machine Cutter Rings

Xingwang Feng¹, Yunxin Wang¹, Jinxin Han¹, Zhipeng Li¹, Likun Jiang^{1,2} and Bin Yang^{1,*}

- ¹ Collaborative Innovation Center of Steel Technology, University of Science and Technology Beijing, Beijing 100083, China; m202221336@xs.ustb.edu.cn (X.F.); d202110597@xs.ustb.edu.cn (Y.W.); g20209277@xs.ustb.edu.cn (J.H.); m202121294@xs.ustb.edu.cn (Z.L.); d202210624@xs.ustb.edu.cn (L.J.)
- ² Advance Materials Institute, Qilu University of Technology (Shandong Academy of Science), Jinan 250353, China
- * Correspondence: byang@ustb.edu.cn

Abstract: Owing to the non-uniform distribution of chemical composition and temperature during the heat treatment process, the residual stress and deformation of the workpiece emerge as crucial factors requiring consideration in managing the service performance and lifespan of shield machine cutter rings crafted from H13 steel. Considering H13 steel with titanium microalloying as the research object for the shield machine cutter ring, we simulate the quenching process using Deform-3D. The temperature field, phase transformation, stress evolution, and deformation amount after quenching are analyzed. The results demonstrate a strong agreement between the simulation and experimental results, offering valuable insights for optimizing the heat treatment process and enhancing the overall performance of shield machine cutter rings.

Keywords: H13 steel; titanium microalloying; shield machine cutter ring; residual stress; numerical simulation



Citation: Feng, X.; Wang, Y.; Han, J.; Li, Z.; Jiang, L.; Yang, B. Numerical Simulation and Experimental Verification of the Quenching Process for Ti Microalloying H13 Steel Used to Shield Machine Cutter Rings. *Metals* **2024**, *14*, 313. <https://doi.org/10.3390/met14030313>

Academic Editors: Andrzej Gontarz and Grzegorz Winiarski

Received: 27 January 2024

Revised: 4 March 2024

Accepted: 5 March 2024

Published: 7 March 2024



Copyright: © 2024 by the authors. Licensee MDPI, Basel, Switzerland. This article is an open access article distributed under the terms and conditions of the Creative Commons Attribution (CC BY) license (<https://creativecommons.org/licenses/by/4.0/>).

1. Introduction

Quenching stands as one of the predominant industrial heat treatments for enhancing the mechanical properties of metals, including their strength and toughness, among others. The quenching process encompasses various coupling phenomena, particularly within the realm of physical metallurgy, which pose challenges in terms of control and prediction, diminishing the probability of the dimensional accuracy of processed components being impacted [1].

The quenching process produces residual stress in steel, stemming from the thermal stress generated by substantial temperature gradients and the austenite–martensite phase transformation within the component [2–6]. The magnitude of this stress is contingent upon the material’s chemical composition [7].

The significant internal stress generated by a specific process or phenomenon can manifest in either a tensile or compressive state, and its impact on the workpiece can be either advantageous or detrimental. Compressive residual stress on the component’s surface is beneficial to the material. Conversely, tensile stress may lead to fatigue performance issues in the components [8,9], which is undesirable during the service life of the workpiece [7].

H13 steel is a hot working die steel that is frequently used for the production of cutter rings for shield machines. Nonetheless, it tends to exhibit failure modes such as chipping and wear because these cutter rings are often exposed to high-strength rock extrusion and impact during their usage, leading to increased economic expenses. Therefore, enhancing its strength and toughness while ensuring its high hardness and excellent wear resistance has become a pressing concern in prolonging the service life of H13 steel cutter rings and decreasing the associated construction expenses.

Microalloying is a method of adding microalloying elements such as Ti [10,11], Nb [12,13], V [14], and rare earth elements [15–19] to steels to enhance the mechanical properties of the steels. Among these options, the addition of Ti to steel leads to the formation of fine and dispersed TiC particles. These particles pin the austenite grain boundary and hinder its growth, as well as enhance both the strength and toughness of the steel [10]. To investigate the impact of titanium microalloying on the quenching residual stress of H13 steel and offer insights for optimizing the heat treatment process of cutter rings, we employ numerical simulation technology to analyze the temperature and stress evolution of the Ti microalloying H13 steel (referred to as H13-Ti steel) used to shield machine cutter rings when subjected to the quenching process. The accuracy of these simulation results is validated through experimental verification.

2. Database Establishment, Numerical Procedure, Simulation Control

2.1. Database Establishment of H13-Ti Steel

To assess the volume fractions of different phases and stress evolution of cutter rings during quenching, it is imperative to establish a material database for H13-Ti steel (Beijing Goal Science Technology Co., Ltd., Beijing, China) with high integrity and reliability. Table 1 presents the chemical composition of H13-Ti. This database must include essential information such as the flow stress, strain, thermophysical and thermomechanical parameters, and equations describing microstructural evolution. Ignoring the influence of Ti on the thermal physical parameters, including Young's modulus, Poisson's ratio, the latent heat of phase transformation, density, etc., they is obtained from the material database of H13 steel attached to Deform-3D V11.0 software, as illustrated in Figure 1.

Table 1. Chemical composition of H13-Ti steel (mass fraction, %).

C	Cr	Mo	Si	V	Mn	S	Ti	Fe
0.42	4.96	1.23	0.96	0.99	0.43	<0.003	0.13	Bal.

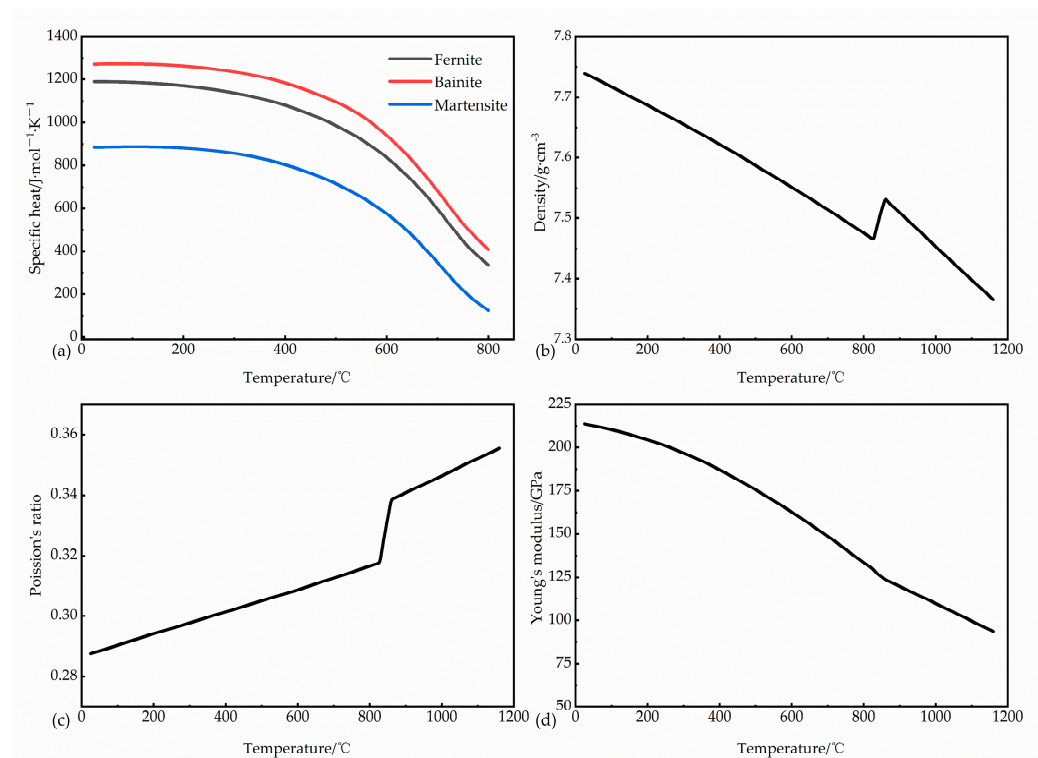


Figure 1. Thermophysical parameters of H13-Ti steel: (a) Specific heat; (b) Density; (c) Poisson's ratio; (d) Young's modulus.

In order to obtain more accurate simulation results for the heat treatment, the TTT (Time–Temperature Transformation) diagram and CCT (Continuous Cooling Transformation) diagram of the H13-Ti steel are calculated using thermodynamic calculation software JMatpro V7.0 following austenitization at 1040 °C, as depicted in Figure 2. The accuracy of the software’s calculation results is validated through numerous experiments [20–22]. The initial transformation temperatures for bainite, ferrite, and martensite are determined as 478.7 °C, 849.9 °C, and 302.6 °C, respectively. The temperature is 266.5 °C at a 50% martensitic transformation, and 182.7 °C at a 90% martensitic transformation. The addition of titanium to H13 steel enhances the efficiency of martensite transformation, resulting in the improved strength and hardness of the material matrix [23]. Using the TTT diagram and the M_s point value, the b and n values in Formula (6), and the ∂ value in Formula (7) are determined.

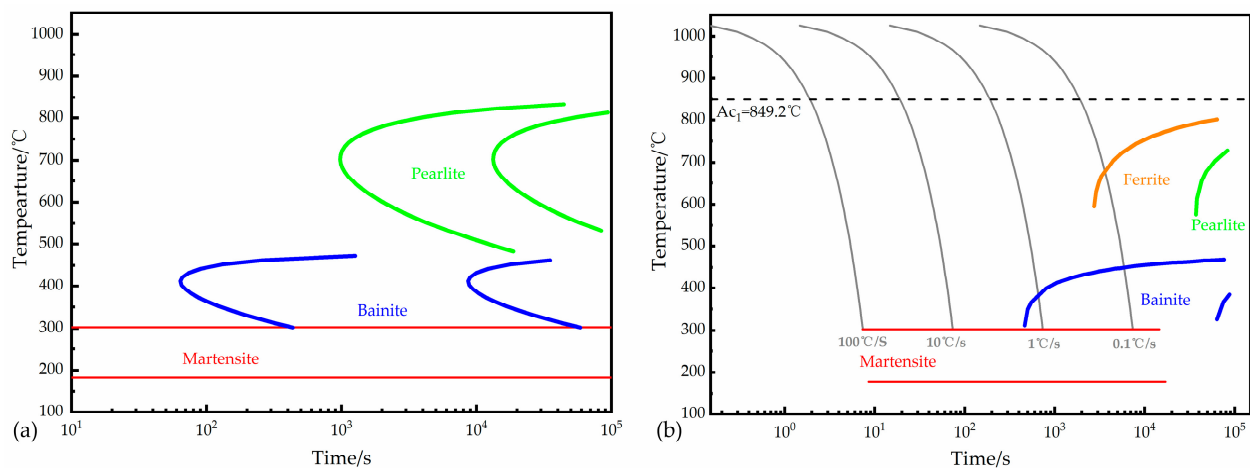


Figure 2. (a) TTT diagram and (b) CCT diagram of H13-Ti steel.

2.2. Numerical Procedure

2.2.1. Determination of Temperature Distribution

Fourier’s law constitutes the fundamental principle of heat conduction. By applying Fourier’s and energy conservation laws, one can derive the corresponding differential equation for heat conduction in a rectangular coordinate system.

$$\rho \cdot C_p \frac{\partial T}{\partial t} = \lambda \left(\frac{\partial^2 T}{\partial x^2} + \frac{\partial^2 T}{\partial y^2} + \frac{\partial^2 T}{\partial z^2} \right) + q \quad (1)$$

where T is the temperature of the workpiece, which is a function of the coordinates and time; x , y , and z denote the coordinate direction; t is the time of heat treatment; λ represents the thermal conductivity of H13-Ti steel; ρ is the density; C_p is the specific heat at constant pressure; and q is the latent heat of phase change [24].

The differential equation of heat conduction provides a general framework for describing heat conduction processes. However, each specific heat conduction process occurs under distinct conditions, distinguishing it from others. Thus, for a particular heat conduction process, supplementary conditions are required to delineate their unique characteristics, including geometric, physical, initial, and boundary conditions. In this study, we investigate the quenching process within the heat treatment regimen of the cutter ring. The unsteady axisymmetric heat conduction differential equation is employed to depict the temperature distribution. The initial condition presumes a uniform internal temperature across each workpiece, with temperature values set at room temperature (25 °C) and the

austenitizing temperature, respectively. The boundary condition corresponds to the third boundary condition, which is expressed as follows:

$$-\lambda \left. \frac{\partial T}{\partial n} \right|_s = H_K (T_w - T_f) \quad (2)$$

where H_K represents the convective heat transfer coefficient, T_w denotes the surface temperature of the workpiece, and T_f is the medium temperature [25,26].

2.2.2. Phase Transformation Kinetics

During the heat treatment process, the volume fractions of different phases in the cutter ring undergo alterations in response to temperature fluctuations. If the initial phase attains the critical transition temperature during heating, austenite phase transformation takes place. A simplified diffusion-type phase transformation model is commonly employed to describe the formation process of austenite. This equation is utilized to calculate the transformation process of ferrite, pearlite, martensite, and bainite to austenite. Moreover, this formula is an approximation based on the strong applicability of diffusion-type phase transformation, enabling the determination of the volume fraction of austenite during austenitizing.

$$V = 1 - e^{\left\{ A \left(\frac{T - T_s}{T_e - T_s} \right)^B \right\}} \quad (3)$$

Here, V is the volume fraction of the austenite phase; T_s and T_e are the starting and finish temperatures of the transition; and T represents the temperature of the workpiece. The material parameters A and B can be determined through the application of Equations (4) and (5) and the TTT diagram. V_s (=0.01) and V_e (=0.99) are the initial and final volume fractions of each phase, and t_s (=0.01) and t_e (=0.99) denote the initiation and completion times of the transition [27].

$$A = -\frac{\ln(1 - V_s)}{t_s^B} \quad (4)$$

$$B = \frac{\ln\{\ln(1 - V_s)/\ln(1 - V_e)\}}{\ln(t_s/t_e)} \quad (5)$$

The Johnson–Mehl–Avrami–Kolmogorov (JMAK) model elucidates the kinetics of isothermal phase transformations by considering the nucleation and growth of new phases. This model is applied to austenite–ferrite, austenite–bainite, and austenite–pearlite diffusion-type phase transformations [28–30].

$$\zeta_i = 1 - e^{(-bt^n)} \quad (6)$$

In this equation, ζ_i denotes the volume fraction of the i phase, t represents the time of isothermal diffusion, b is the phase nucleation rate, and n is the phase growth rate. These are constants, and can be derived from the TTT diagram of the H13-Ti steel at different temperatures. Non-diffusive phase transformations, such as austenite–martensite, are temperature dependent and can be determined using the relationship proposed by Koistinen and Marburger et al. [31].

$$V = 1 - \exp[-\partial(M_s - T)] \quad (7)$$

In this equation, V signifies the volume fraction of martensitic transformation, M_s is the starting temperature of martensitic transformation, T is the quenching temperature, and ∂ is the kinetic constant of the phase transition, obtainable from the TTT diagram of the H13-Ti steel.

2.2.3. Determination of Stress and Strain Field

In the elastic–plastic model, the influence of the strain value, strain rate and temperature is considered in the calculation of plastic flow stress. The differential of total strain ($d\varepsilon$) comprises elastic ($d\varepsilon_e$), plastic ($d\varepsilon_p$), thermal ($d\varepsilon_{th}$), phase transformation ($d\varepsilon_{tr}$), and transformation plastic ($d\varepsilon_{tp}$) strains, as defined by Equation (8):

$$d\varepsilon = d\varepsilon_e + d\varepsilon_{th} + d\varepsilon_p + d\varepsilon_{tr} + d\varepsilon_{tp} \quad (8)$$

The plastic flow stress is expressed by Equation (9):

$$\bar{\sigma} = \bar{\sigma}(\varepsilon, \dot{\varepsilon}, T) \quad (9)$$

where $\bar{\sigma}$ represents the plastic flow stress, ε denotes strain, $\dot{\varepsilon}$ signifies the strain rate, and T stands for temperature.

2.3. Simulation and Experiment Process

(1) Deform-3D finite element software [32] is utilized to simulate the quenching process of the cutter ring, incorporating coupling calculations encompassing temperature, phase transition, and elastic–plastic modules. To ensure the accuracy of the simulation, the temperature, phase transition, and other workpiece information are imported into the subsequent step after completing the calculation of the previous step, resulting in the creation of a new file for the next computational step [33,34].

(2) The three-dimensional model diagram depicted in Figure 3a is established based on the actual geometric shape and size of the cutter ring of the shield machine. Then, it is saved as an STL format file compatible with Deform-3D.



Figure 3. (a) Dimensional diagram of shield machine cutter ring; (b) simulation model, finite element meshing and the scheme of heat transfer; and (c) the object of the shield machine cutter ring.

(3) The initial material information of the cutter ring is defined and input, and the temperature of the workpiece, the cooling medium, and the heat transfer coefficient are specified. As shown in Figure 3b, all outer surfaces of the cutter ring serve as a heat exchange boundary to facilitate information exchange between the phase change module and the temperature module.

(4) The workpiece is modeled as an elastic–plastic body and divided into tetrahedral grids using the adaptive meshing method. The time step is adjusted based on the holding time and cooling rate at various heat treatment stages to guarantee the accuracy and

convergence of the re-operation process. The grid count totals 50,000 units, and the node count is 9998, as illustrated in Figure 3b. The grid count is deemed sufficient to ensure calculation accuracy and convergence.

(5) Phase transition information is derived from TTT and CCT diagrams (isothermal transition curve), and the phase transition data are input. Subsequently, the stress distribution and deformation of the cutter ring are determined utilizing the thermophysical parameters of H13-Ti steel.

(6) During the process of analyzing the results, representative points on the cross-section of the entire cutter ring are utilized for analysis, as depicted in Figure 4.

(7) A sample measuring $10 \times 10 \times 10$ mm is cut along the edge of the blade at position P1 (as shown in Figure 4) using an electric spark wire-cutting machine. Subsequently, any burrs are removed by grinding and polishing with sandpaper. The high-power microscopic morphology of the samples is observed utilizing the ZEISS SUPRATM55 scanning electron microscope (SEM).

3. Results and Discussion

To elucidate the temperature, volume fractions of different phases, stress evolution, and deformation at various positions of the cutter ring, the particle tracking method is employed to analyze the simulation results. The particle sampling identification points are illustrated in Figure 4, where P1, P2 and P3 represent, respectively, the near-surface layer at the cutter ring's edge, the center of the tool, and the near-surface layer at the cutter ring's back, closer to the center than P1.

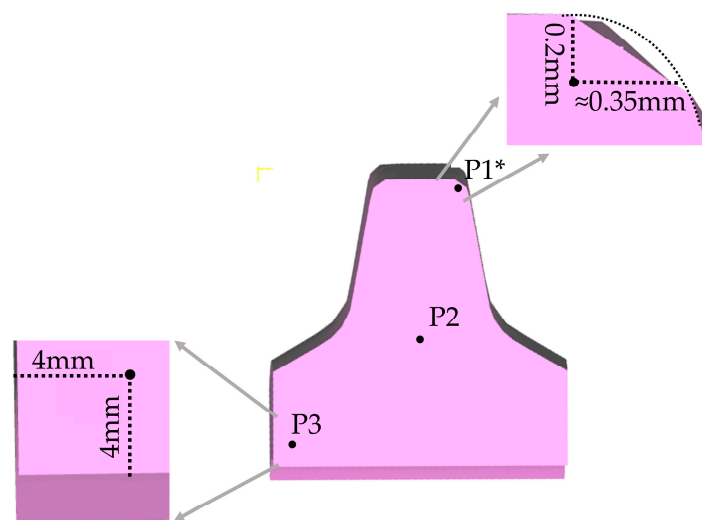


Figure 4. Sampling points of particle data. * The arc of the blade P1 point is simplified to a straight line edge in the simulation process.

3.1. Temperature and Structure Field

The simulation modeled the evolution of the temperature field in the cutter ring as it is heated from room temperature to 1040 °C, followed by complete austenitization and quenching in water. The representative results are shown in Figure 5. The temperature gradient around the cutter ring edge gradually shifts towards the center. Temperature variations at the sampling point during the extraction heating process are depicted in Figure 6a. Point P2 (the center of the tool) exhibits a slower heating rate and a lower local temperature compared to points P1 and P3. However, the temperature variance between P1 and P3 remains insubstantial throughout. As the heating duration extends, the temperature gradient between the surface and the center diminishes, leading to a more uniform temperature field. Figure 6b illustrates the temperature variation over time during the cooling process. Quenching results in the faster cooling of the workpiece exterior compared to the slower cooling of the core. The observed inflection point arises from

martensitic transformation occurring at this temperature (302.6 °C, Figure 2), with point P2 exhibiting the most pronounced inflection. On one hand, the direct contact between the workpiece exterior and the cooling medium accelerates heat transfer. On the other hand, the surface layer undergoes phase transition during cooling, releasing latent heat transferred to the core, thereby maintaining a higher core temperature and slowing the overall cooling rate.

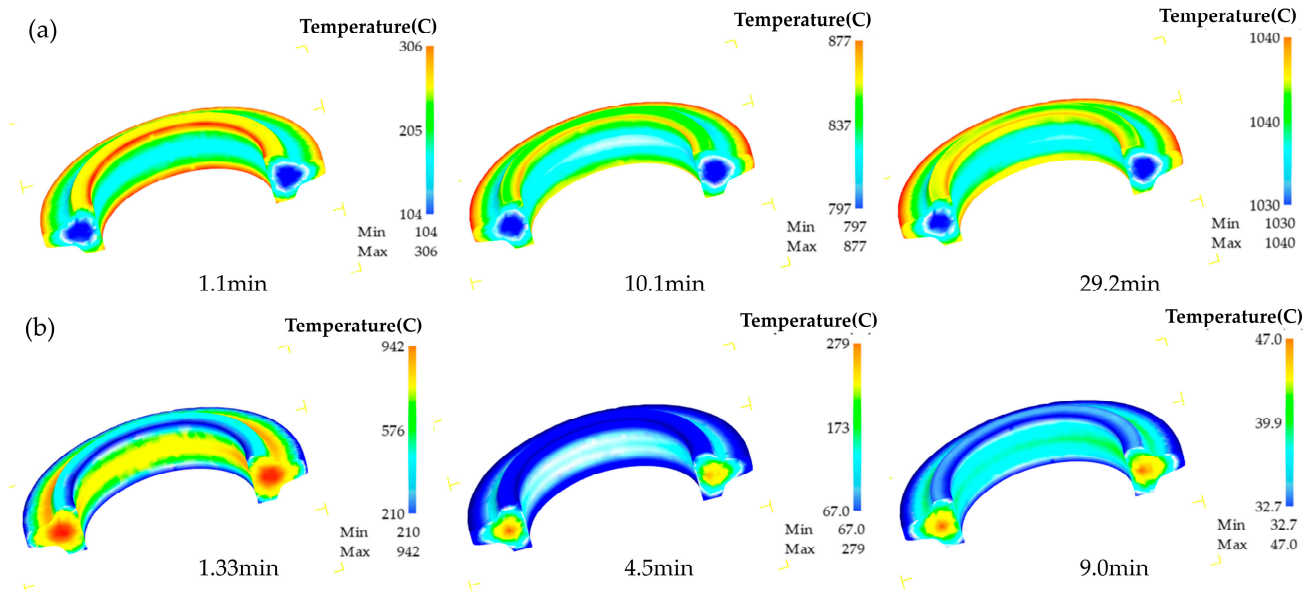


Figure 5. Temperature fields of H13-Ti steel for (a) heating process for 1.1, 10.1 and 29.2 min, respectively, and (b) water cooling process for 1.33, 4.5, 9.0 min, respectively.

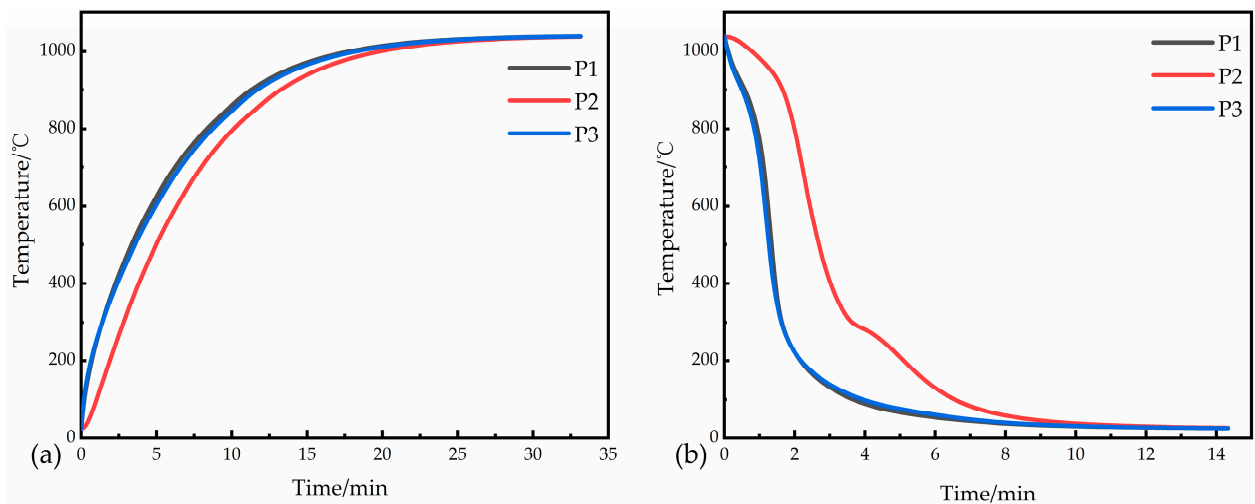


Figure 6. Temperature–time curves of H13-Ti steel in (a) the heating process and (b) the water cooling process.

The curve depicting the evolution of the workpiece’s volume fractions of the austenite and martensite phases over time during the heat treatment process is presented in Figures 7 and 8, presenting the distributions of austenite and martensite structures at a particular time during the heat treatment process. From Figure 6a, it shows that external points P1 and P3 experience a higher temperature rate, leading to a preferential transformation into the austenite phase. With the extension of the heating time, the austenite structure manifests from the surface to the core. Towards the conclusion of the heating process at

29.2 min, the workpiece has undergone substantial austenitization, with only a minimal presence of ferrite.

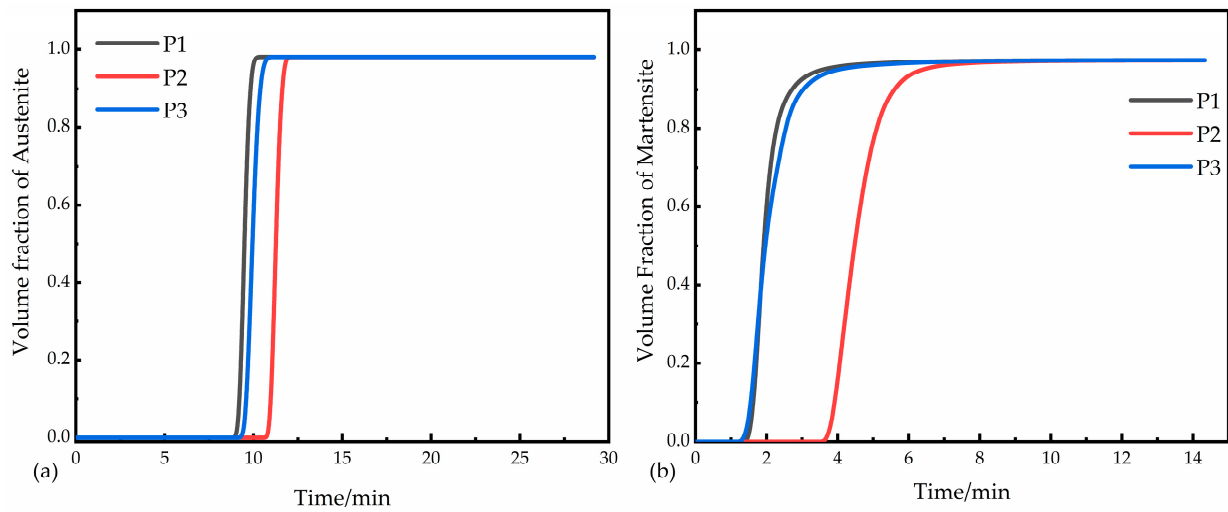


Figure 7. Variations in austenite and martensite phases as a function of time under (a) the heating process and (b) the water cooling process.

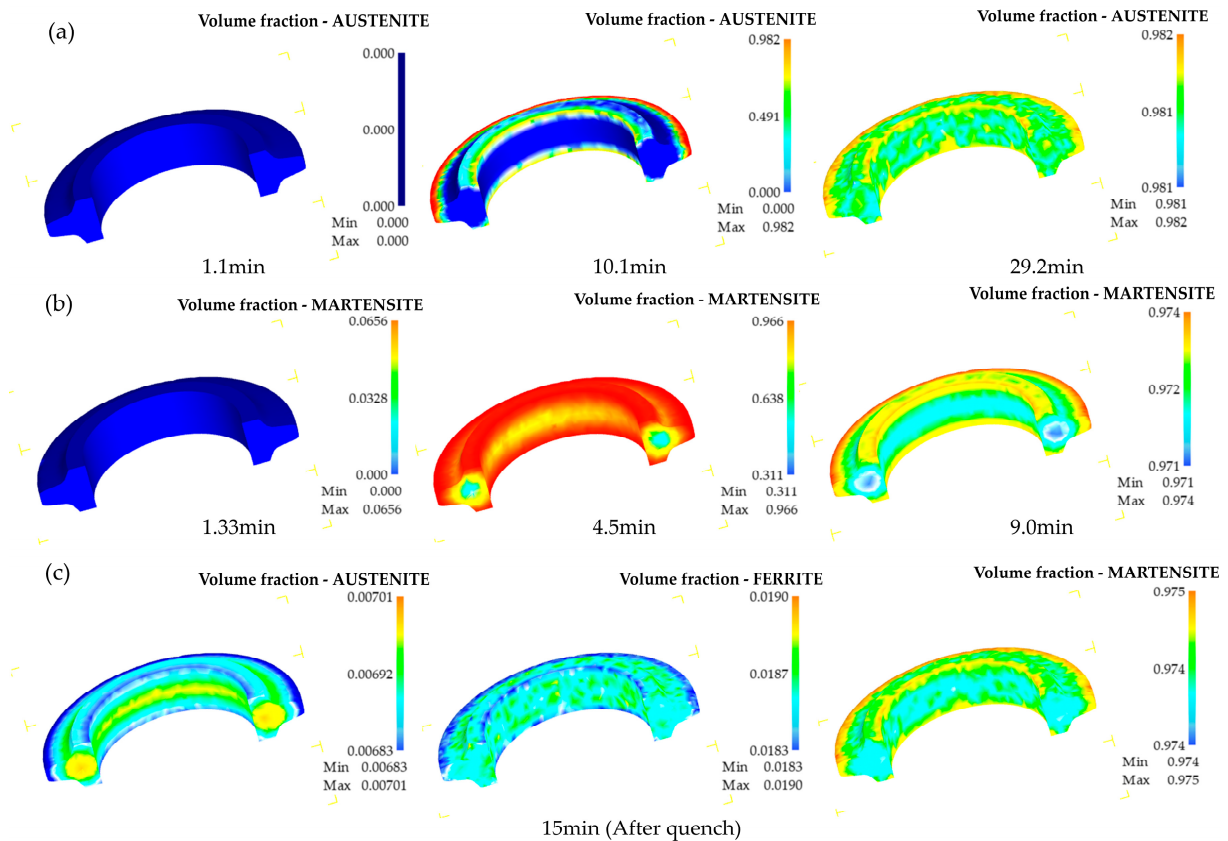


Figure 8. The volume fractions of different phases during (a) heating process for 1.1, 10.1, and 29.2 min, respectively, and (b) water cooling for 1.33, 4.5, 9.0 min, and (c) 15 min, respectively.

The results of the simulation of the volume fractions of different phases during the water cooling process of the workpiece are presented in Figure 8b,c. When the quenching time is 1.33 min, the surface temperature (Figure 5b) initially falls below the martensitic transformation point (302.6 °C, Figure 2), leading to the appearance of the martensite

structure. As the cooling time increases, the martensitic phase begins to manifest in the core after 4 min. Meanwhile, the volume fraction of martensite in the surface layer reaches approximately 0.966. After 15 min of water cooling, the cutter ring is fully cooled. Figure 8b,c reveal a minimal presence of austenite structure, with a volume fraction of approximately 0.007, indicating a complete transformation. The workpiece exhibits minimal bainite content, with the volume fraction of martensite being as high as 0.974. Following quenching, the cutter ring predominantly comprises martensite, with a negligible presence of other structural components.

3.2. Stress and Displacement Amount Analysis

The stress in the heat treatment process primarily arises from the thermal stress induced by substantial temperature variations and structural stress stemming from structural transformation [5,35]. These combined stresses constitute the internal stress within the cutter ring during the heat treatment process. The quality of the workpiece is predominantly influenced by the distribution of internal stress during the quenching process. To enhance our comprehension of stress evolution, a simulation study on the cutter ring during the quenching water cooling process is conducted. Von Mises stress and axial stress are derived from the simulation results, as illustrated in Figure 9, where the axial stress (σ_{yy}) represents the y-direction, as depicted in Figure 3a,b. Figure 9a depicts the trend of Von Mises stress during the quenching process of the cutter ring. In quenching stage 1 (S-1), The Von Mises stress at the surface layer (P1) gradually increases, while the stresses in the near-surface layer (P3) and the center (P2) also increase accordingly. Subsequently, in quenching stage 2 (S-2), the stress increases rapidly, reaching a maximum of 1044 MPa (P1), and then gradually decreases until the stress values become stable towards the end of quenching. In quenching stage 3 (S-3), the stress values at the surface (P1) and near the surface stabilize, while the Von Mises stress at the center tends to stabilize with a slow and small amplitude. After quenching, the stress magnitude at the blade edge (P1) is the highest, at approximately 380 MPa. Figure 9b depicts the trend of axial stress variation during the quenching process of the cutter ring. In S-1, the surface (P1) exhibits tensile stress along the Y-axis (axial direction), with the most complex stress variations occurring in S-2. In S-3, the tensile stress gradually diminishes. The trend of stress variation at point P3 resembles that of point P1, albeit slightly delayed. In S-1, the stress state at point P2 contrasts with that at points P1 and P3, while in S-2 and S-3, it aligns with the trend observed at P1. After quenching, the axial stress at the blade edge (P1) reaches its maximum value, measuring 78.32 MPa.

In S-1, a significant temperature disparity exists between the workpiece surface and the quenching medium, resulting in rapid heat dissipation and a consequent rapid reduction in the surface temperature. Heat conduction dissipates the temperature difference within the core, resulting in a slower rate of temperature decrease compared to the surface. While the surface temperature decreases rapidly, it experiences significant shrinkage, whereas the core undergoes comparatively minor shrinkage. Consequently, the surface experiences tensile stress due to the center's resistance to shrinkage forces, while the center undergoes compression. Thus, in Figure 9a (S-1, the Von Mises stress on the surface (P1) increases rapidly, and the stresses in the near-surface (P2) and center (P3) areas increase accordingly. The Von Mises stress in the center is low, and it experiences compressive stress in the axial direction (Figure 9b S-2). In S-2, as depicted in Figures 6c and 7b, the surface layer initially decreases to the M_s temperature, with the preferential occurrence of the martensitic transformation. The phase transition is accompanied by an increase in volume, resulting in stress change. During this period, the stress state evolution becomes complex due to the combined effects of thermal stress and phase transition stress. In Figure 9a S-2, Von Mises stress indicates that the center changes with the stress of the surface layer, initially increasing in stress and then sharply decreasing. In Figure 9b, the axial stress in S-2 transitions from compressive stress to tensile stress. In S-3, the temperature of the workpiece's center drops to the M_s , initiating the martensitic transformation. During the initial period of center

phase transition, thermal stress resulting from temperature fluctuations prevails. So, in Figure 9a S-3, the Von Mises stress at the P2 point gradually increases. Subsequently, the dominant phase transformation stress, induced by the martensitic transformation, leads to the volume of the center expanding. However, the surface impedes the expansion of the center martensite, resulting in a decrease in surface stress (with axial stress becoming compressive) until the conclusion of the quenching process.

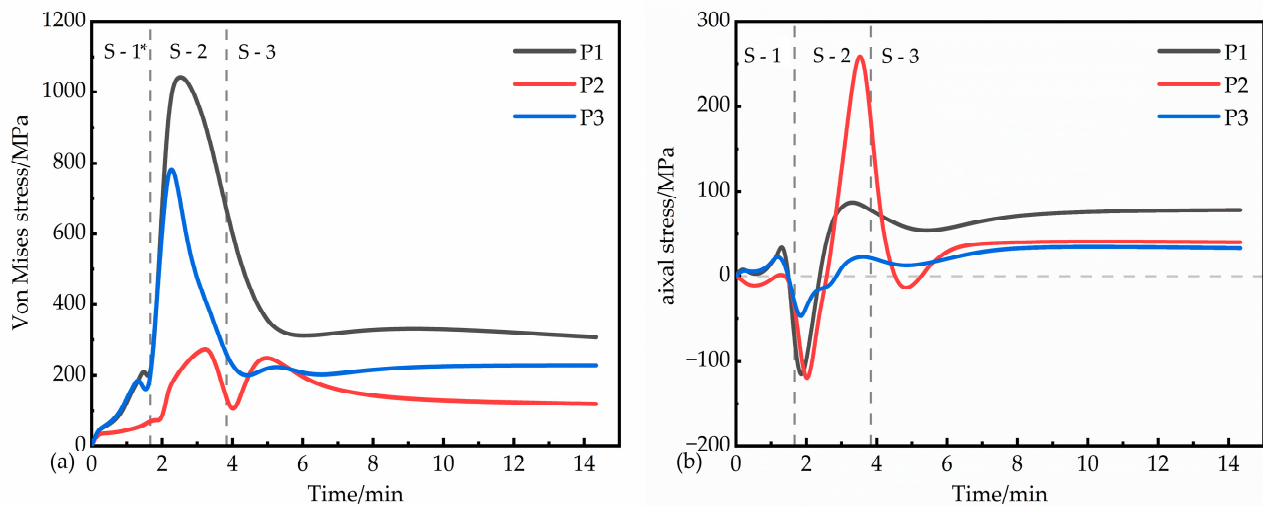


Figure 9. Evolution of (a) Von Mises stress and (b) axial stress of sampling points during quenching process. * S-1 (quenching stage 1) is no martensitic transformation, S-2 (quenching stage 2) is martensitic transformation in the surface layer but no phase transformation in the center, S-3 (quenching stage 3) is martensitic transformation in the center to the end of quenching.

Based on the aforementioned analysis, it is evident that employing water-cooled quenching for the cutter ring induces significant internal stress, which is subsequently transformed into and retained as residual stress after cooling. This results in substantial residual tensile stress during usage, elevating the likelihood of deformation and cracking. Such conditions are unfavorable for achieving the prolonged life and cost-effectiveness of the shield machine cutter ring. Consequently, the subsequent cooling procedure should be chosen to ensure uniform stress distribution and its suitability for the cutter ring's intricate working conditions.

According to the simulation results, the edge of the cutter ring experiences the highest stress, potentially compromising the overall performance. Further analysis focuses on post-heat treatment displacement. Figure 10a depicts the total displacement curve of a sampling point over time during heat treatment, Figure 10b illustrates the total displacement field, and Figure 10c displays the displacement field in the y-direction (axial direction). Throughout the quenching process, the total displacement shows a pattern of initial increase, stabilization, subsequent decrease, gradual rise, and eventual stabilization. Following the 1040 °C holding period, P1 experiences its maximum displacement, at approximately 4.35 mm. During the water cooling stage, the displacement rapidly decreases to 1.79 mm, undergoes a gradual increase to 2.29 mm, and eventually stabilizes. Subsequent to water cooling, significant distortion is observed at the upper surface of the cutter ring (P1 side). Due to constraints imposed by the heat treatment furnace's plane, axial displacement primarily occurs along the normal direction of the cutter ring axis. After water cooling, the largest displacement, measuring 1.68 mm, occurs at the blade edge.

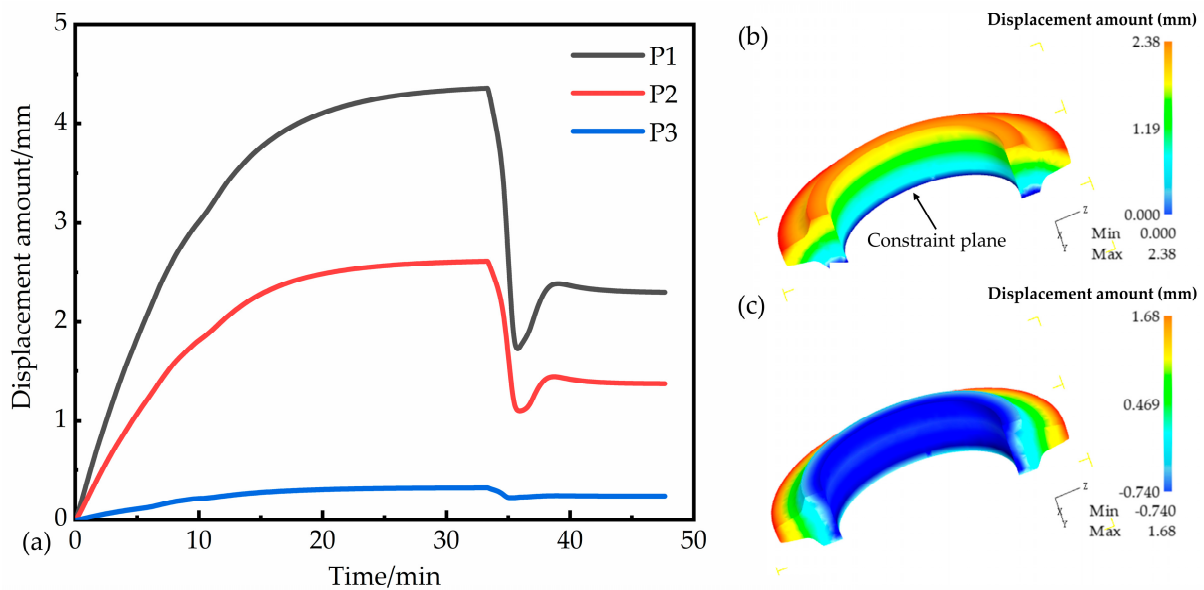


Figure 10. (a) The total displacement evolution curves of sampling points during heat treatment process; (b) total displacement field; (c) displacement field in the axial direction.

3.3. Experimental Verification

Based on the simulation parameters mentioned above, a verification experiment is conducted. After quenching, a sample is cut from the cutter ring and subjected to microstructural examination. The microstructural analysis is depicted in Figure 11. It reveals a predominantly martensitic microstructure, with the majority of undissolved large carbides precipitating along the grain boundary. Some small carbides precipitate within the grain. This characterization provides valuable insights into the microstructural composition after the quenching process, particularly the presence and distribution of carbides within the martensitic matrix.

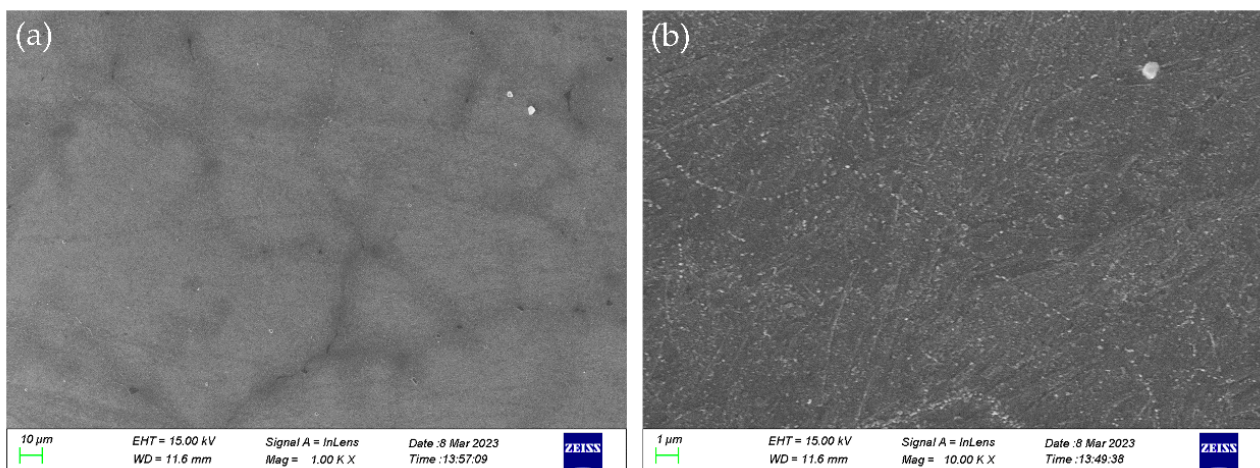


Figure 11. SEM microstructures of the H13-Ti steel at different magnifications after water cooling for 15 min. (a) 1000 \times , (b) 10,000 \times .

4. Conclusions

This paper establishes a heat treatment database for H13 steel after titanium microalloying using Deform-3D. Additionally, it simulates the evolution of the temperature, phase transformation, and stress field for the shield cutter ring during water-cooled quenching. The simulation results indicate that water quenching induces higher internal stress in the cutter ring, posing challenges to the longevity and cost-effectiveness demanded by

shield machine cutter rings. Consequently, it is imperative to opt for a cooling process characterized by uniform stress distribution and suitable for complex working conditions. A robust agreement is achieved between the simulation and experiment results, affirming the accuracy of the database and the reliability of the simulation outcomes.

Author Contributions: Conceptualization, B.Y. and X.F.; methodology, X.F. and Y.W.; software, X.F., Y.W. and Z.L.; validation, J.H., Y.W. and L.J.; formal analysis, Z.L. and J.H.; investigation, Z.L. and L.J.; data curation, X.F., Y.W., J.H., Z.L. and L.J.; writing—original draft, X.F.; writing—review and editing, B.Y., Y.W., J.H., Z.L. and L.J.; supervision, B.Y., X.F., Y.W., J.H. and Z.L.; project administration, B.Y. and X.F.; funding acquisition, B.Y. All authors have read and agreed to the published version of the manuscript.

Funding: This research was funded by the Key R&D Program of Shandong Province (No. 2021CXGC010209), the Fundamental Research Funds for the Central Universities (No. FRF-BD-23-01), and Nuclear Technology Support Center, State Administration of Science, Technology and Industry for National Defence, and Young Scientists Fund of the National Natural Science Foundation of China (No. 52101066).

Institutional Review Board Statement: Not applicable.

Informed Consent Statement: Not applicable.

Data Availability Statement: The original contributions presented in the study are included in the article, further inquiries can be directed to the corresponding author.

Conflicts of Interest: The authors declare no conflicts of interest.

References

1. Tikhe, O.; Doiphode, P.; Nichul, U.; Singh, R.; Hiwarkar, V. Development of Optimized Mechanical Properties of AISI 4340 Steel: Role of Quenching and Partitioning Process. *Met. Mater. Int.* **2023**, *29*, 2216–2227. [[CrossRef](#)]
2. da Silva, A.D.; Pedrosa, T.A.; Gonzalez-Mendez, J.L.; Jiang, X.; Cetlin, P.R.; Altan, T. Distortion in quenching an AISI 4140 C-ring—Predictions and experiments. *Mater. Des.* **2012**, *42*, 55–61. [[CrossRef](#)]
3. Nallathambi, A.K.; Kaymak, Y.; Specht, E.; Bertram, A. Sensitivity of material properties on distortion and residual stresses during metal quenching processes. *J. Mater. Process. Technol.* **2010**, *210*, 204–211. [[CrossRef](#)]
4. Grum, J.; Božič, S.; Zupančič, M. Influence of quenching process parameters on residual stresses in steel. *J. Mater. Process. Technol.* **2001**, *114*, 57–70. [[CrossRef](#)]
5. Samuel, A.; Prabhu, K.N. Residual Stress and Distortion during Quench Hardening of Steels: A Review. *J. Mater. Eng. Perform.* **2022**, *31*, 5161–5188. [[CrossRef](#)]
6. Wang, R.; Jiang, H.; Shao, W.; Yang, S.; Sun, X.; Cao, J.; Zhen, L. Quenching induced residue stress in M50 steel ring: A FEM simulation. *J. Mater. Res. Technol.* **2023**, *24*, 5298–5308. [[CrossRef](#)]
7. Lopez, R.; Garcia-Pastor, F.; Maldonado-Reyes, A.; Jiménez-Gómez, M.A.; Rodríguez-García, J.A. Analysis of the effect of immersion rate on the distortion and residual stresses in quenched SAE 5160 steel using FEM. *J. Mater. Res. Technol.* **2019**, *8*, 5557–5571. [[CrossRef](#)]
8. Brzozza, M.; Kaymak, Y.; Specht, E.; Bertram, A. Simulation of the Distortion of Long Steel Profiles during Cooling. *J. Appl. Mech.* **2007**, *74*, 427–437. [[CrossRef](#)]
9. Gür, C.H.; Tekkaya, A.E. Numerical investigation of non-homogeneous plastic deformation in quenching process. *Mater. Sci. Eng. A* **2001**, *319–321*, 164–169. [[CrossRef](#)]
10. Wang, S.; Gao, Z.; Wu, G.; Mao, X. Titanium microalloying of steel: A review of its effects on processing, microstructure and mechanical properties. *Int. J. Miner. Metall. Mater.* **2022**, *29*, 645–661. [[CrossRef](#)]
11. An, X.; Tian, Y.; Wang, H.; Shen, Y.; Wang, Z. Suppression of Austenite Grain Coarsening by Using Nb–Ti Microalloying in High Temperature Carburizing of a Gear Steel. *Adv. Eng. Mater.* **2019**, *21*, 1900132. [[CrossRef](#)]
12. Ray, A.; Bhadeshia, H.K.D.H. Niobium in Microalloyed Rail Steels. In *HSLA Steels 2015, Microalloying 2015 & Offshore Engineering Steels 2015*; Springer: Cham, Switzerland, 2016; pp. 33–39.
13. Sun, L.-y.; Liu, X.; Xu, X.; Lei, S.-w.; Li, H.-g.; Zhai, Q.-j. Review on niobium application in microalloyed steel. *J. Iron. Steel Res. Int.* **2022**, *29*, 1513–1525. [[CrossRef](#)]
14. Dong, F.; Venezuela, J.; Li, H.; Shi, Z.; Zhou, Q.; Chen, L.; Chen, J.; Du, L.; Atrens, A. Effect of vanadium and rare earth microalloying on the hydrogen embrittlement susceptibility of a Fe-18Mn-0.6C TWIP steel studied using the linearly increasing stress test. *Corros. Sci.* **2021**, *185*, 109440. [[CrossRef](#)]
15. Wang, J.-f.; Wang, L.-z.; Chen, C.-y.; Wang, X.; Zhao, F. Effect of rare earth on primary carbides in H13 die steel and their addition method: A review. *J. Iron. Steel Res. Int.* **2024**. [[CrossRef](#)]

16. Chen, Y.; Ye, C.; Chen, X.; Zhai, Q.; Hu, H. Effect of Alloying and Microalloying Elements on Carbides of High-Speed Steel: An Overview. *Metals* **2024**, *14*, 175. [[CrossRef](#)]
17. Chen, R.; Wang, Z.; He, J.; Zhu, F.; Li, C. Effects of Rare Earth Elements on Microstructure and Mechanical Properties of H13 Die Steel. *Metals* **2020**, *10*, 918. [[CrossRef](#)]
18. Jiang, Z.; Wang, P.; Li, D.; Li, Y. Effects of rare earth on microstructure and impact toughness of low alloy Cr-Mo-V steels for hydrogenation reactor vessels. *J. Mater. Sci. Technol.* **2020**, *45*, 1–14. [[CrossRef](#)]
19. Zhu, J.; Lin, G.T.; Zhang, Z.H.; Xie, J.X. The martensitic crystallography and strengthening mechanisms of ultra-high strength rare earth H13 steel. *Mater. Sci. Eng. A* **2020**, *797*, 140139. [[CrossRef](#)]
20. Saunders, N.; Guo, U.K.Z.; Li, X.; Miodownik, A.P.; Schillé, J.P. Using JMatPro to model materials properties and behavior. *JOM* **2003**, *55*, 60–65. [[CrossRef](#)]
21. Ma, Q.; Li, X.; Xin, R.; Liu, E.; Gao, Q.; Sun, L.; Zhang, X.; Zhang, C. Thermodynamic calculation and machine learning aided composition design of new nickel-based superalloys. *J. Mater. Res. Technol.* **2023**, *26*, 4168–4178. [[CrossRef](#)]
22. Wang, J.; Li, X.; Yi, K.; Elmi, S.A. Research on the Temperature and Thermal Stress of the Roll Quenching Process of Thin Plates. *Metals* **2024**, *14*, 83. [[CrossRef](#)]
23. Kaoumi, D.; Liu, J. Deformation induced martensitic transformation in 304 austenitic stainless steel: In-situ vs. ex-situ transmission electron microscopy characterization. *Mater. Sci. Eng. A* **2018**, *715*, 73–82. [[CrossRef](#)]
24. Simsir, C.; Gür, C.H. Simulation of Quenching. In *Handbook of Thermal Process Modeling of Steels*; Routledge: Abingdon, UK, 2009; pp. 341–425.
25. Sugianto, A.; Narazaki, M.; Kogawara, M.; Shirayori, A.; Kim, S.-Y.; Kubota, S. Numerical simulation and experimental verification of carburizing-quenching process of SCr420H steel helical gear. *J. Mater. Process. Technol.* **2009**, *209*, 3597–3609. [[CrossRef](#)]
26. Li, H.; Zhao, G.; Huang, C.; Niu, S. Technological parameters evaluation of gas quenching based on the finite element method. *Comput. Mater. Sci.* **2007**, *40*, 282–291. [[CrossRef](#)]
27. Kang, S.-H.; Im, Y.-T. Three-dimensional thermo-elastic-plastic finite element modeling of quenching process of plain-carbon steel in couple with phase transformation. *Int. J. Mech. Sci.* **2007**, *49*, 423–439. [[CrossRef](#)]
28. Cahn, J.W. Transformation kinetics during continuous cooling. *Acta Metall.* **1956**, *4*, 572–575. [[CrossRef](#)]
29. Çetinel, H.; Toparlı, M.; Özsoyeller, L. A finite element based prediction of the microstructural evolution of steels subjected to the Tempcore process. *Mech. Mater.* **2000**, *32*, 339–347. [[CrossRef](#)]
30. Reti, T.; Fried, Z.; Felde, I. Computer simulation of steel quenching process using a multi-phase transformation model. *Comput. Mater. Sci.* **2001**, *22*, 261–278. [[CrossRef](#)]
31. Koistinen, D.P.; Marburger, R.E. A general equation prescribing the extent of the austenite-martensite transformation in pure iron-carbon alloys and plain carbon steels. *Acta Metall.* **1959**, *7*, 59–60. [[CrossRef](#)]
32. Fluhner, J. *DEFORMIM-3D Version 5.0 User's Manual*; Corporation SFT, Ed.; Corporation SFT: Columbus, OH, USA, 2005.
33. Wang, S.; Yang, B.; Zhang, M.; Wu, H.; Peng, J.; Gao, Y. Numerical simulation and experimental verification of microstructure evolution in large forged pipe used for AP1000 nuclear power plants. *Ann. Nucl. Energy* **2016**, *87*, 176–185. [[CrossRef](#)]
34. Qian, D.; Pan, Y. 3D coupled macro-microscopic finite element modelling and simulation for combined blank-forging and rolling process of alloy steel large ring. *Comput. Mater. Sci.* **2013**, *70*, 24–36. [[CrossRef](#)]
35. Esfahani, A.K.; Babaei, M.; Sarrami-Foroushani, S. A numerical model coupling phase transformation to predict microstructure evolution and residual stress during quenching of 1045 steel. *Math. Comput. Simul.* **2021**, *179*, 1–22. [[CrossRef](#)]

Disclaimer/Publisher's Note: The statements, opinions and data contained in all publications are solely those of the individual author(s) and contributor(s) and not of MDPI and/or the editor(s). MDPI and/or the editor(s) disclaim responsibility for any injury to people or property resulting from any ideas, methods, instructions or products referred to in the content.